Electronic Supplementary Material (ESI) for Energy & Environmental Science.

Adjacent Fe Site Boosts Electrocatalytic Oxygen Evolution of Co Site in Single-Atom-Catalyst through a Dual-Metal-Site Design

Changli Chen,[a,g] Mingzi Sun,[b] Fang Zhang,[c] Haijing Li,[d] Mengru Sun,[a] Pin Fang, [a] Tinglu Song,[e] Wenxing Chen,[a] Juncai Dong,[d] Brian Rosen,[f] Pengwan Chen,[a] Bolong Huang,[b]* Yujing Li [a]*

a. Beijing Key Laboratory of Construction Tailorable Advanced Functional Materials and Green Applications, School of Materials Science and Engineering, Beijing Institute of Technology, Beijing 100081, P. R. China
b. Department of Applied Biology and Chemical Technology, The Hong Kong Polytechnic University, Hung Hom, Kowloon, Hong Kong SAR, China
c. Analysis and Testing Center, Beijing Institute of Technology, Beijing Institute of Technology, Beijing 100081, P. R. China
d. Beijing Synchrotron Radiation Facility, Institute of High Energy Physics, Chinese Academy of Sciences, Beijing 100049, P. R. China
e. Experimental Center of Advanced Materials, School of Materials Science and Engineering, Beijing Institute of Technology, Beijing 100081, P. R. China
f. Department of Materials Science and Engineering, Tel Aviv University, Tel Aviv-Yafo, Ramat Aviv, 69978001, Israel
g. School of Chemistry and Chemical Engineering, Qilu University of Technology (Shandong Academy of Sciences), Jinan 250353, P. R. China

Contents

1. Materials and Synthesis Section

1.1 Materials

Ferrous chloride tetrahydrate ($FeCl_2 \cdot 4H_2O$, Alfa), Cobalt chloride hexahydrate ($CoCl_2 \cdot 6H_2O$, Alfa) Melamine ($C_3H_6N_6$, Acros), Tripolythionic acid ($C_3H_6N_3S_3$, Acros)， Hexadecyl trimethyl ammonium bromide (CTAB, $C_{19}H_{42}BrN$, Sigma-aldrich) Poly(ethylene imine) (PEI, Alfa).

1.2 Synthesis of the Co/Fe-SNC catalyst

The Co/Fe-SNC catalysts were synthesized with different Co/Fe ratios to investigate the OER catalytic performance. Firstly, 0.1 g CTAB was dissolved in 20 mL of DMF, and then, 0.5 g melamine and 0.5 g thiocyanuiric acid was added to the solution and stirred at room temperature for 0.5 h. Secondly, a certain proportion of $FeCl_2 \cdot 4H_2O$ and $CoCl_2 \cdot 6H_2O$ were dropped into the above mix solution simultaneously and then stir at room temperature for 2 h. Thirdly, the 0.2 g PEI (600 MW) was added into the above solution and stirred at room temperature for overnight. Finally, 40 mL of H_2O was added with a stirring for 15 min intensely. The obtained suspension was centrifuged to obtain the bottom precipitate, and then was dried in an air oven at 80 °C for 12 h. Residual powder was calcined at 550 °C for 2 h and then 800 °C (3 °C min^{-1}) for 2 h in tube furnace under N_2 atomsphere. The reference Fe-SNC and Co-SNC were synthesized in the same method. The pre-catalysts with different ratios and pyrolysis temperatures were referred to Table S1.

2. Characterization Methods

X-ray diffraction (XRD) patterns were recorded by using a Bruker D8 Focus equipped with Cu Kα radiation at a scanning rate of 5° min^{-1}. Scanning electron microscopy (SEM) images were obtained by using a Hitachi S-4800 SEM. High-angle annular dark-field scanning transmission electron microscopy (HAADF-STEM) images and EDS elemental mapping images were obtained by using a FEI Titan G2 microscope equipped with a probe spherical aberration corrector and a Bruker SuperX EDX detector, operated at 200 kV. The pore structure and specific surface area of the pre-catalysts were analyzed by nitrogen (N_2) adsorption and desorption isotherms (Micromeritics ASAP 2460). The metal content (Fe and Co) and organic components (C, N, O, S) of the catalysts were analyzed using inductively coupled plasma emission spectrometry (ICP-OES, Agilent ICP-OES 730) and elemental analysis (Elementar, vario E1 cube). Raman spectra of the powder samples were recorded with a Renishaw inVia Raman microscope with a laser excitation wavelength of 532 nm. X-ray photoelectron spectroscopy (XPS) was performed using Thermo ESCALAB 250Xi. Continuous-wave electron Paramagnetic Resonance (EPR) spectra collected on the catalysts conducted on Burker A300-10/12 under the applied potentials. The Fe, Co K-edge XAFS spectra were acquired at beamline 1W1B station of the Beijing Synchrotron Radiation Facility, China. The Fe, Co K-edge XAFS data were recorded in a fluorescence mode using a Lytle detector. Fe foil, Co foil, Fe phthalocyanine (FePc) and Co phthalocyanine (CoPc) were used as references. The acquired EXAFS data were processed according to the standard procedures using the Athena and Artemis implemented in the IFEFFIT software packages. The EXAFS spectra were obtained by subtracting the post-edge background from the overall absorption and then normalizing with respect to the edge-jump step. Subsequently, the $\chi(k)$ data were Fourier transformed to real (R) space using a handing window (dk=1.0 $Å^{-1}$) to separate the EXAFS contributions from different coordination shells. To obtain the quantitative structural parameters around central atoms, least-squares curve parameter fitting was performed using the Artemis module of IFEFFIT software packages.

3. Electrochemical Measurements

3.1 Purification of KOH Electrolyte

The 1.0 M KOH was purified using high purity cobalt nitrate salts following a reported procedure.1-2 0.8 g of $Co(NO_3)_2 \cdot 6H_2O$ was dissolved in 5 mL of ultrapure water, which was added to 20 mL of 1 M KOH. The obtained $Co(OH)_2$ precipitate was centrifuged and washed three times with ultrapure water. Then, the $Co(OH)_2$ precipitate was suspended into 50mL 1.0 M KOH, and the mixture was mechanically agitated overnight to absorb the Fe impurities. The resultant brown suspension was centrifuged, and the obtained supernatant is retained to obtain Fe-free electrolyte.

3.2 The catalyst-modified electrode preparation

The catalyst ink was prepared by mixing 145 uL of isopropanol, 145 uL of water, 10uL of 5 wt% Nafion solution, and 5 mg of catalysts. The ink was sonicated for at least 1h. The 10 uL of the ink was uniformly loaded onto a glassy carbon electrode (GC, freshly polished, 0.19625 cm^2), or carbon cloth electrode (CC, washed by water, acetone, and ethanol, respectively, 1 cm^2), respectively. The electrodes were dried at the room temperature before measurements.

3.3 OER activity testing

Linear sweep voltammogram (LSV) curves were obtained at a scan rate of 2 mV s^{-1} after conducting fifty cyclic voltammograms (CVs) at a scan rate of 200 mV s^{-1} in O_2-saturated 1.0 M KOH. Tafel plots were obtained from LSVs and the electrochemical impedance spectroscopy (EIS) was conducted in the range of 10 kHz to 0.01 Hz at an applied potential of 1.60 V vs. RHE. The pre-catalysts were coated on the 1 cm^2 carbon paper for long-term stability and tested by the galvanostatic method. All data were 95% *IR* (*I* stand for current and *R* stands for resistance)-corrected and shifted to the reversible hydrogen electrode (RHE) scale by calibrating the Hg/HgO reference electrode using the equation: $E_{vs.\,RHE} = E_{vs.\,Hg/HgO} + E^{\theta}_{vs.\,Hg/HgO} + 0.0591pH$.

3.4 Electrochemical surface area (ECSA)

Electrochemical capacitance measurements are used to determine the active surface area of the catalyst. To calculate the electrochemical capacitance, the potential was swept between 1.2-1.3 V vs. RHE five cycles at the applied scan rates. The measured capacitive currents are plotted as a function of the scan rate and a linear fit determined the double layer capacitance (C_{dl}). The electrochemical active surface area can be calculated using the following equation[1]:

$$Cs = \frac{\int IdV}{vmV} \quad \text{Equation S1}$$

$$ECSA = \frac{C_{dl}}{C_S} \quad \text{Equation S2}$$

where Cs is the specific capacitance (F g^{-1} cm^{-2}), I is the current (A), v is the scan rate (mV/s), m is the mass of catalyst (g), and V is the potential window (V). C_s is calculated by CV in Figure S16. C_{dl} is calculated by CVs in Figure S15.

3.5 Evaluation of Metal Active Site Density (MASD)

Metal mass-specific active site density can be calculated using the following equations：

$$MASD = \frac{A * N_A}{n * v * F * n_{TM}} \quad \text{Equation S3}$$

where A is the absolute area of CV curves, N_A is the Avogadro number ($6.022*10^{23}$ mol^{-1}), n is the number of electrons, v is the scan rate (10 mV s^{-1}), F is the Faraday constant (96485 C mol^{-1}), and n_{TM} is the metal amount of substance of the electrocatalyst loading (0.167 mg) on glassy carbon electrode.

3.6 The calculation of turnover frequency (TOF)

The turnover frequency (TOF) is evaluated by the following equation:

$$TOF = \frac{i}{4 * F * ASD} * N_A \quad \text{Equation S4}$$

where i is current (A), N_A is the Avogadro constant (6.022×10^{23} mol^{-1}), 4 is the electron transfer number during OER, and F is the Faraday constant (96485 C mol^{-1}).

3.7 Rotating ring disk electrode test

Rotating ring disk electrode (RRDE) voltammetry was performed with a Pine rotator. The number of electrons transferred as a function of applied potential was calculated using the following relationship[2-4]:

$$n = \frac{4I_{disk}}{I_{disk} + \frac{I_{ring}}{N}} \quad \text{Equation S5}$$

The proportion of H_2O_2 produced during OER was quantified using the following relationship[5]:

$$\%H_2O_2 = \frac{100\frac{2I_{ring}}{N}}{I_{disk} + \frac{I_{ring}}{N}} \quad \text{Equation S6}$$

3.8 O_2-temperature programmed desorption (O_2-TPD)

The adsorptions of O_2 reactant and desorption of intermediates were probed by O_2-temperature programmed desorption (O_2-TPD). The chemisorption O coefficient is employed to assess the oxygen desorption capacity per metal site, which is calculated by Equation S7.

$$Coefficient = \frac{Area}{MASD} \quad \text{Equation S7}$$

3.9 Evaluation of electron transfer capability of modified-electrode initiated by $K_3[Fe(CN)_6]/K_4[Fe(CN)_6]$ pair

All chemical and physical properties of $K_3[Fe(CN)_6]/K_4[Fe(CN)_6]$ are well known as a redox pair, which is easily traceable with optical and electrochemical techniques.[6] The current response of [Fe(CN)6]3-/[Fe(CN)6]4- redox pair is used as a descriptor to assess the electron transfer capability of electrode materials in this work. CV curves were obtained at the various scan rates of 10 mV s^{-1}, 30 mV s^{-1}, 50 mV s^{-1}, 70 mV s^{-1}, 90 mV s^{-1}, and 100 mV s^{-1} after conducting fifty cyclic voltammograms (CVs) at a scan rate of 200 mV s^{-1} in N_2-saturated 0.1 M KCl with 0.05 M $K_3[Fe(CN)_6]/K_4[Fe(CN)_6]$.

4. Theoretical Calculation

To reveal the different OER of the Fe-SNC, Co-SNC, and Co/Fe-SNC, we have introduced density functional theory (DFT) calculations through the CASTEP packages [7]. To describe the accurate exchange-correlation interactions in the calculations, we have chosen the functionals of generalized gradient approximation (GGA) with Perdew-Burke-Ernzerhof (PBE) [8-10]. Meanwhile, we have applied the ultrasoft pseudopotentials and ultrafine quality for the plane-wave basis cutoff

energy as 380 eV. The Broyden-Fletcher-Goldfarb-Shannon (BFGS) algorithm [11] has been utilized for all the energy minimizations. In addition, for all the geometry optimizations, the coarse quality setting of k-points has been applied after the convergence tests. The following convergence criteria have been applied to guarantee high accuracy for geometry optimizations, including the Hellmann-Feynman forces should not exceed 0.001 eV/Å, the total energy difference should be smaller than 5×10^{-5} eV/atom and the inter-ionic displacement needs to be smaller than 0.005 Å, respectively.

5. Figures and Tables

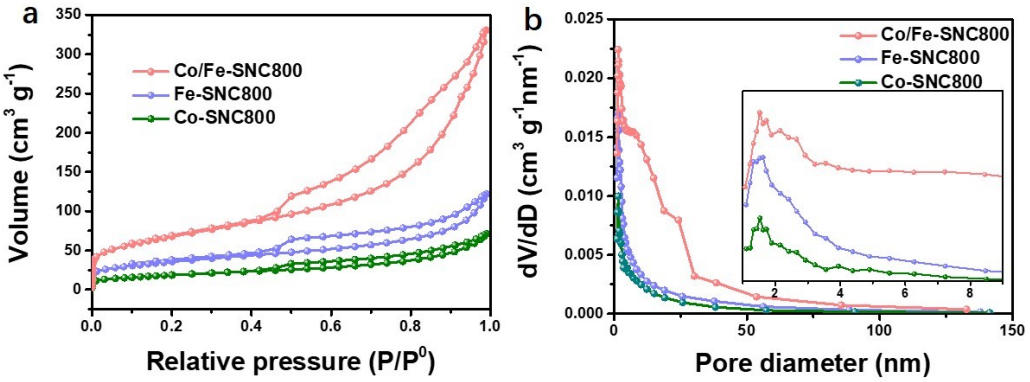

Figure S1. (a) N_2 adsorption-desorption isotherms and (b) pore size distribution of Fe-SNC800, Co-SNC800 and Co/Fe-SNC800.

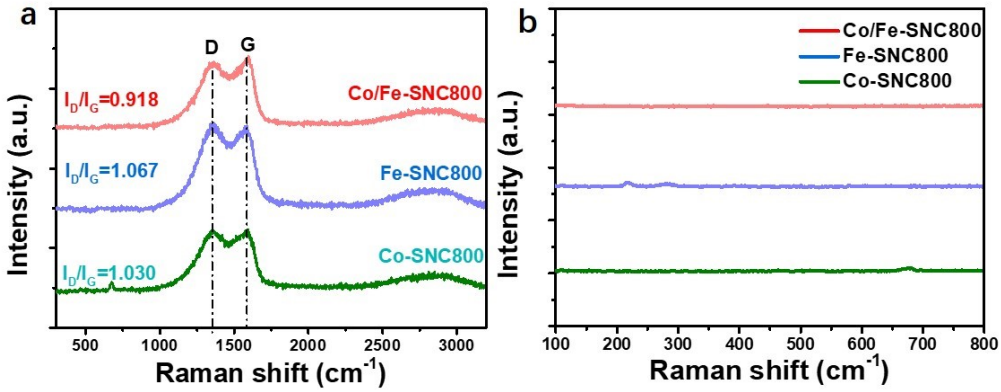

Figure S2. (a) The Raman spectra at wavenumber window between 600-3200 cm^{-1} and (b)the enlarged Raman spectra at low wavenumber window between 200-800 cm^{-1} of Fe-SNC800, Co-SNC800 and Co/Fe-SNC800. The two characteristic peaks centered at 1354 cm^{-1} and 1590 cm^{-1} are corresponding to D-band and G-band in the carbon matrix, respectively. I_D/I_G value is consistent with the defect degree in the carbon, e.g. the higher I_D/I_G value, the higher defect degree.

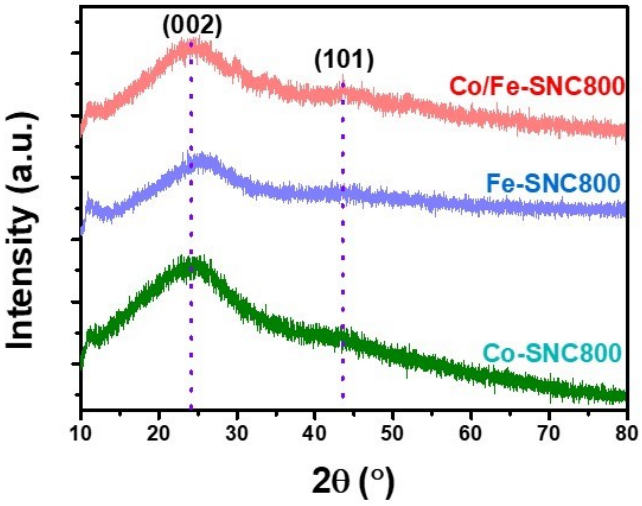

Figure S3. The XRD of Fe-SNC800, Co-SNC800, and Co/Fe-SNC800, respectively.

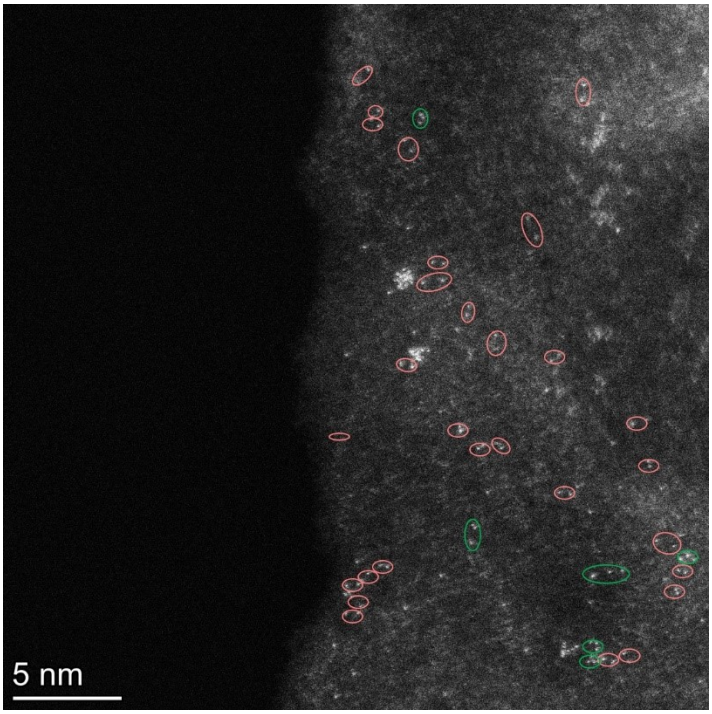

Figure S4. HAADF-STEM images of Co/Fe-SNC800, which is the enlarged original image of Figure 1e with higher resolution. The counting of metallic species and the distribution statistics and carried out based on this image.

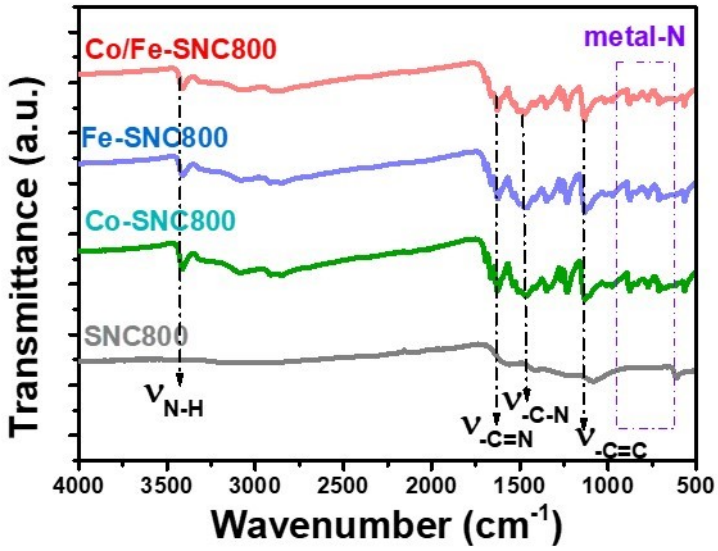

Figure S5. The FTIR spectra of Fe-SNC800, Co-SNC800 and Co/Fe-SNC800. The peaks around ~3418, 1576, 1464, and 1145 cm^{-1} are attributed to N-H, -C=N, -C-N and -C=C stretching vibration, respectively. Compared with FTIR spectra of the metal-based catalysts to SNC800, the -C=N and -C-N stretching is shifted toward higher frequency, demonstrating an obvious interaction of coordination of the N with Fe or Co.

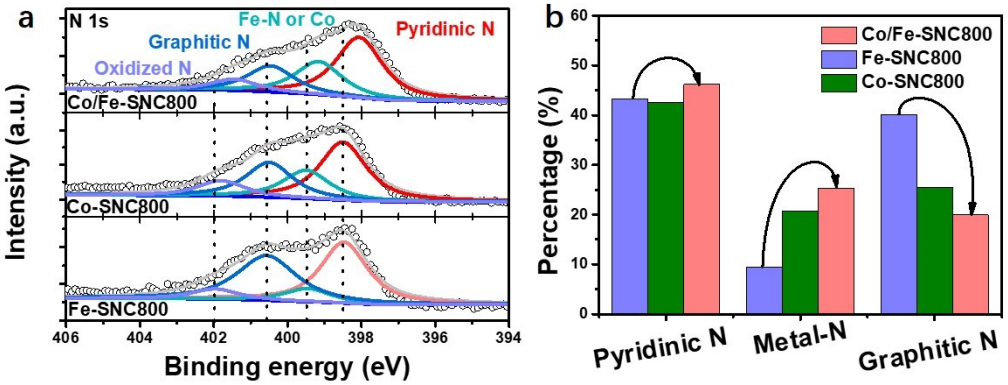

Figure S6. (a) The high-resolution N 1s XPS spectra and (b) the percentage of various N species of Fe-SNC800, Co-SNC800 and Co/Fe-SNC800. The high-resolution XPS N 1s spectrum could be deconvoluted into pyridinic N (398.3 ± 0.3 eV), metal- N (399.5 ± 0.3 eV), graphitic N (400.3 ± 0.3 eV), and oxidized N (401.8 ± 0.3 eV), respectively (Figure 2b).[12]

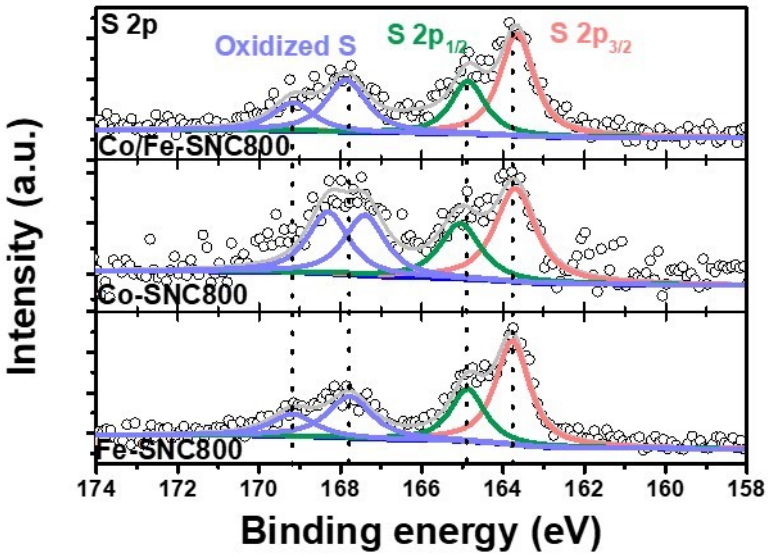

Figure S7. (a) The high-resolution S 2p XPS spectra of Fe-SNC800, Co-SNC800 and Co/Fe-SNC800. The peaks at 163.5 and 165.0 eV are attributed to the S $2p_{3/2}$ and S $2p_{1/2}$ derived from -C-S-C- coordination.

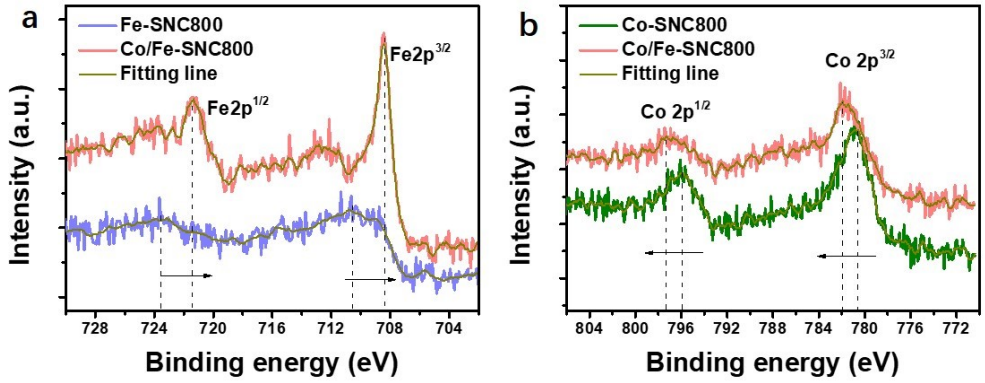

Figure S8. The XPS spectra of Fe 2p and Co 2p in the Fe-SNC800, Co-SNC800 and Co/Fe-SNC800, respectively.

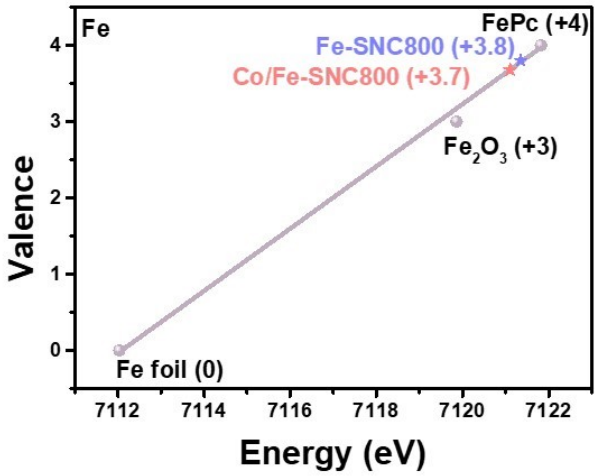

Figure S9. The valence analysis of Fe element in the catalysts along with the reference materials derived from the XAFS data.

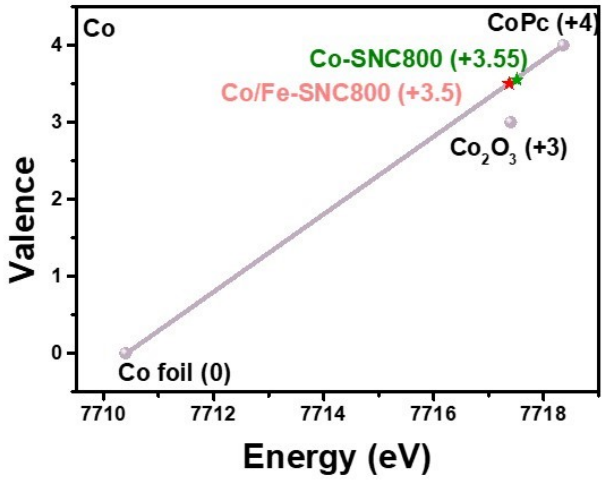

Figure S10. The valence analysis of Co element in the catalysts along with the reference materials derived from the XAFS data.

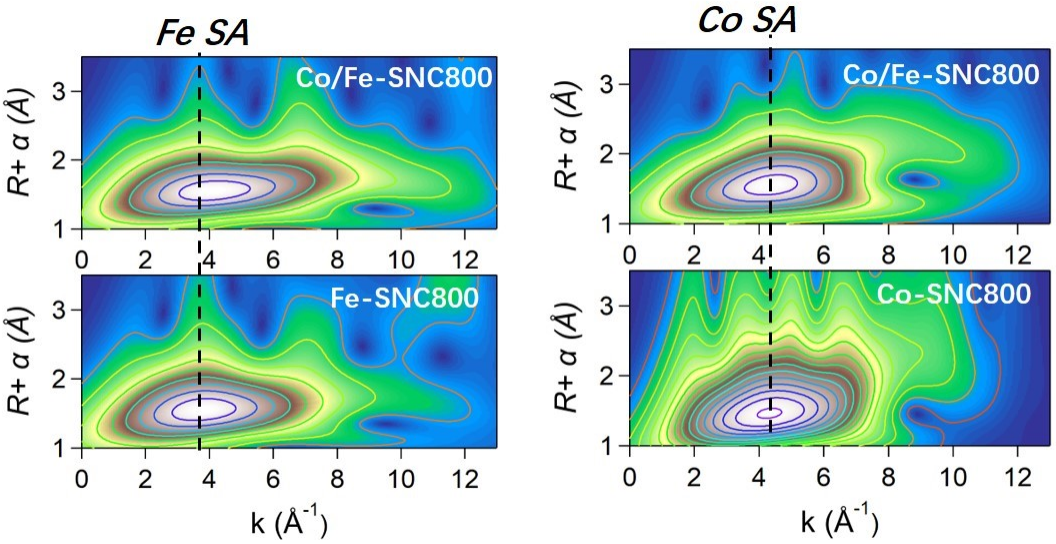

Figure S11. The wavelet transforms of the Fe-SNC800, Co-SNC800 and Co/Fe-SNC800, respectively.

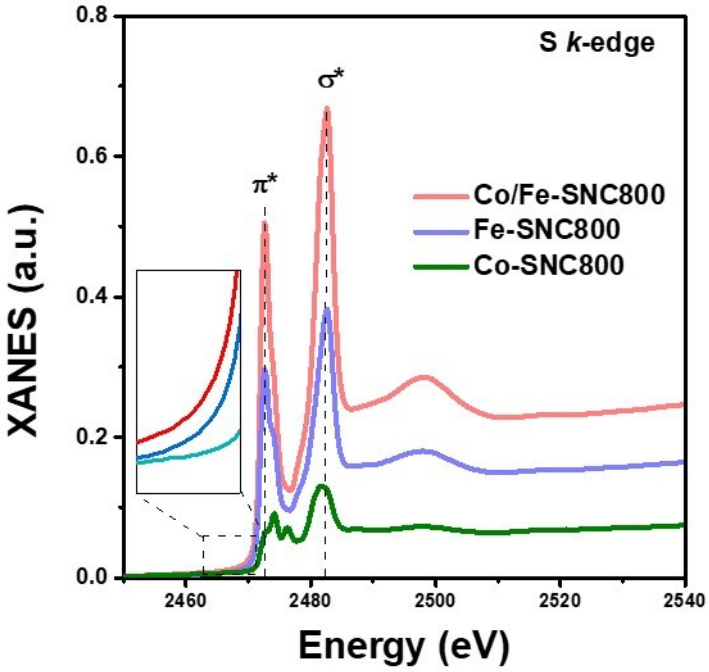

Figure S12. S k-edge NEXAFS spectra of Fe-SNC800, Co-SNC800 and Co/Fe-SNC800, respectively.

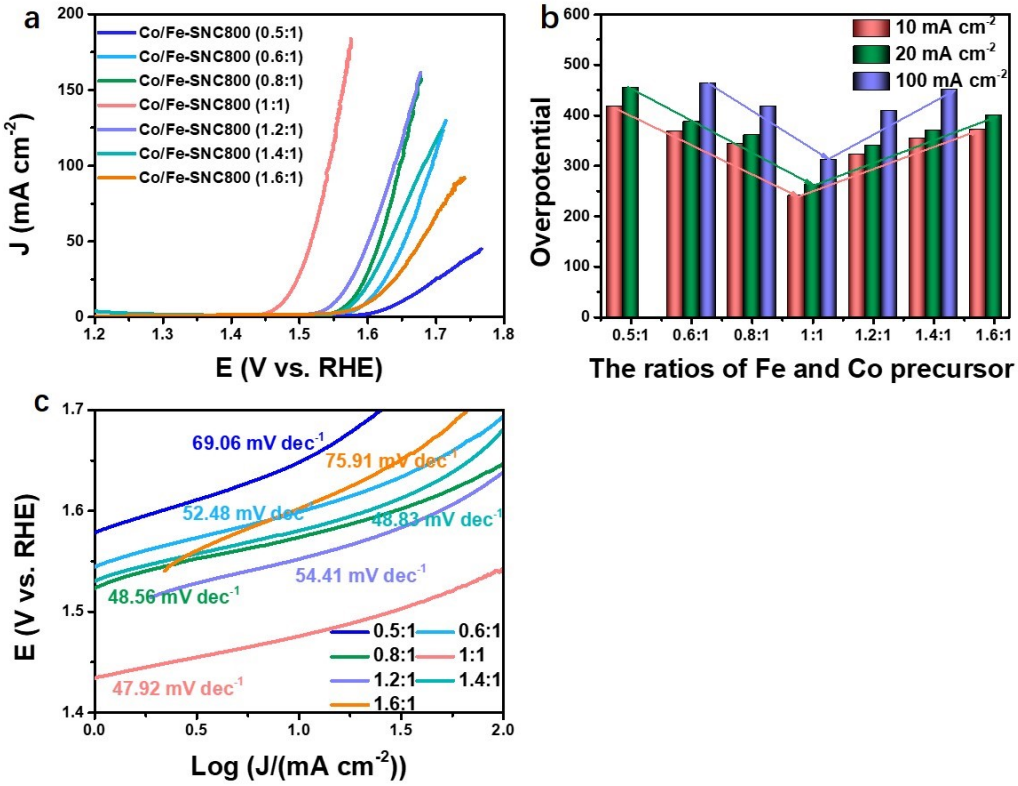

Figure S13. The different ratios of Co/Fe precursor. (a) LSV curves at 1600 rpm; (b) the overpotential of the catalysts at 10, 20, and 100 mA cm^{-2}, respectively; (c) The Tafel plots.

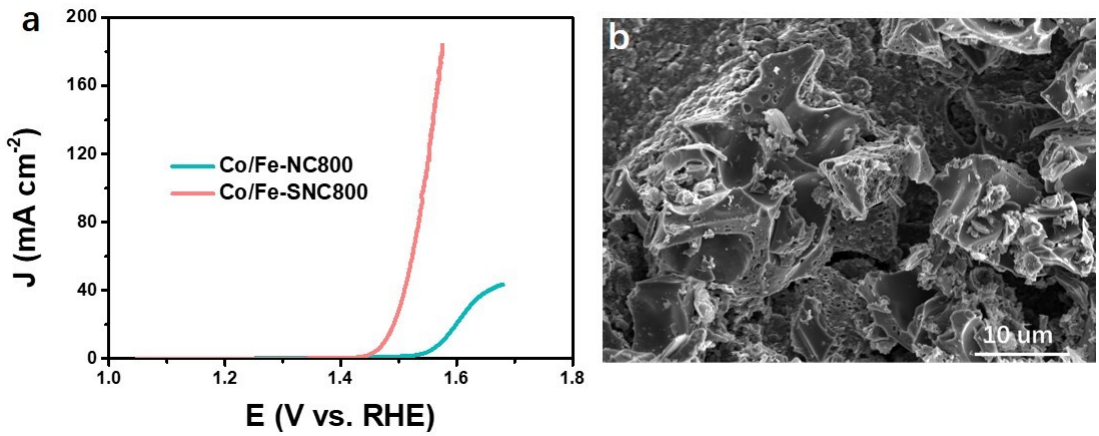

Figure S14. (a) LSV curves of Co/Fe-NC800 and Co/Fe-SNC800 at 1600 rpm, respectively; (b) SEM image of the Co/Fe-NC800.

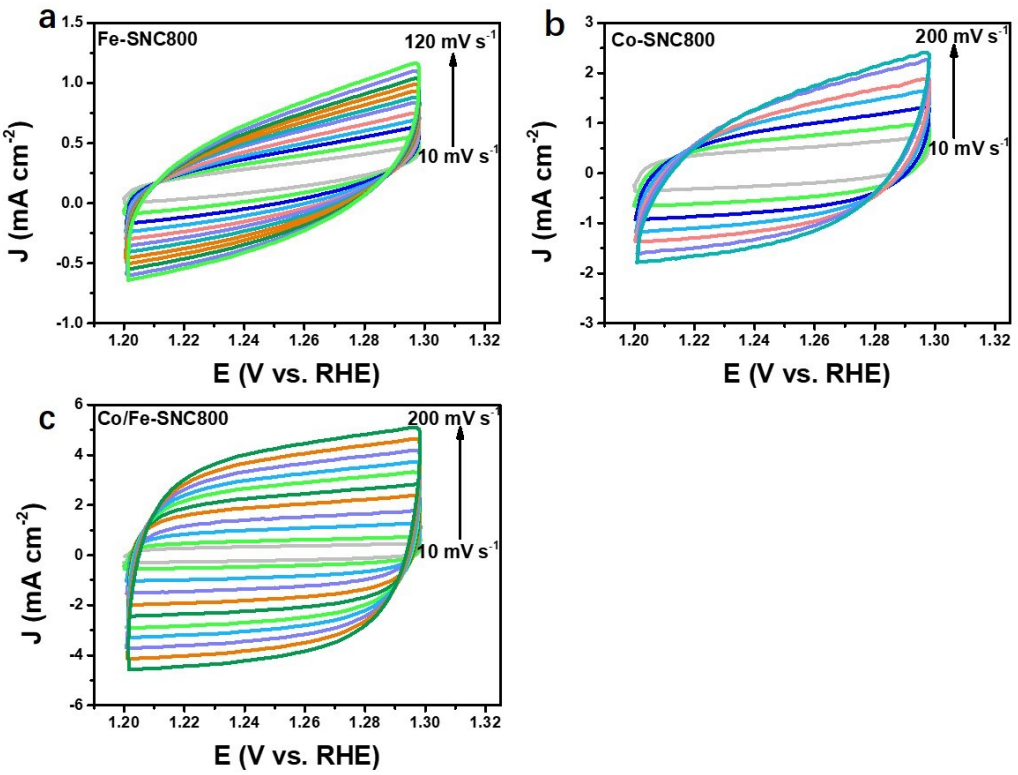

Figure S15. The CV curves (Potential ranging from 1.2-1.3 V with non-Faraday current) of Fe-SNC800, Co-SNC800, and Co/Fe-SNC800 at various scan rates.

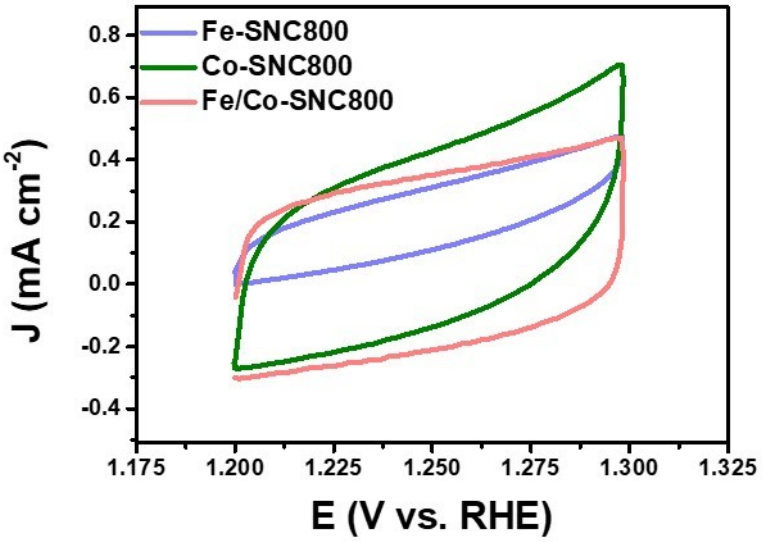

Figure S16. CV curves of Fe-SNC800, Co-SNC800, and Co/Fe -SNC800 at 10 mV s^{-1}, respectively. The absolute areas of the obtained catalysts are used to calculate the Cs.

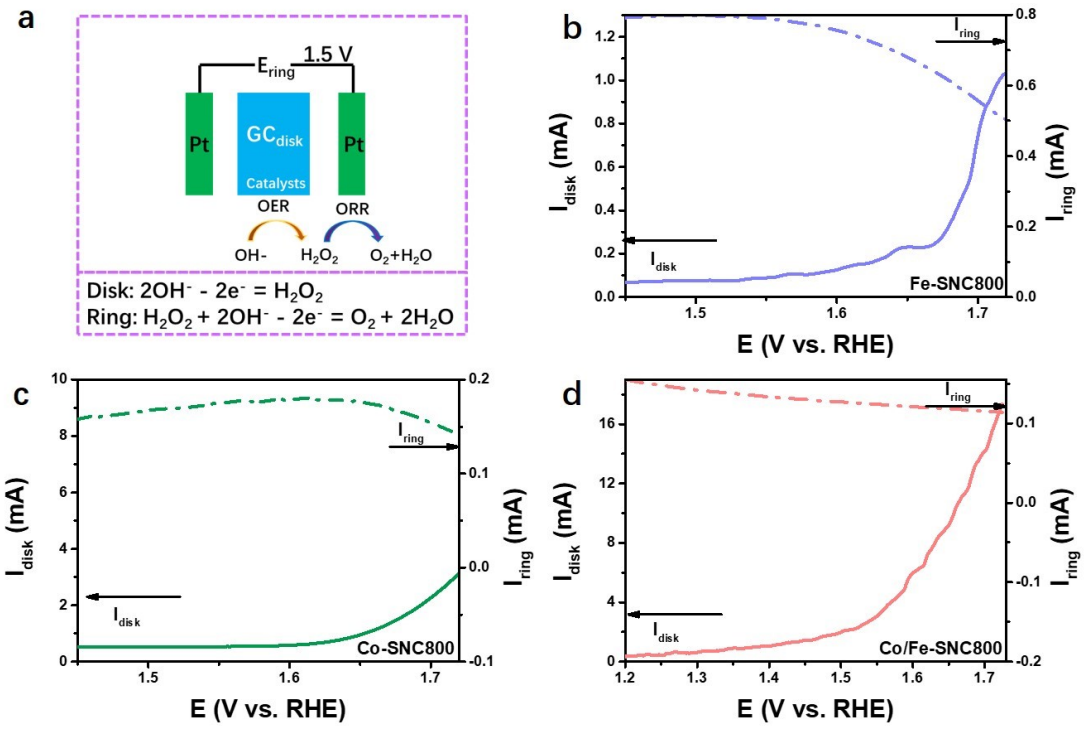

Figure S17. (a) The working mechanism of the RRDE and the simplified reactions at the disk and ring microelectrodes; RRDE curves (The potential of ring electrode: 1.5 V vs. RHE) of OER for (b) Fe-SNC800, (c) Co-SNC800, and (d) Co/Fe-SNC800. Very low I_{disk} and n value (close to 0) of Fe-SNC800 at the potential <1.5 V indicates that Fe-SNC800 has an inefficiency to directly catalyze the OER process to form O_2 or even H_2O_2 unless a particularly large overpotential is applied. In the OER using Co-SNC800 catalyst, the first $2e^-$ stage involves the formation of H_2O_2 on the Co sites at the low overpotential.

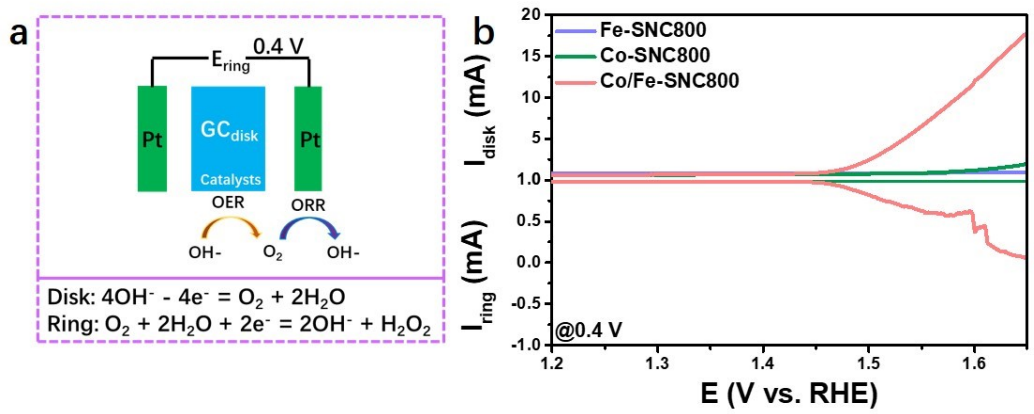

Figure S18. (a) The working mechanism of the RRDE and the simplified reactions at the disk and ring microelectrodes.[13] (b) Ring and disk currents measured in the RRDE configuration (E_{ring} = 0.4 V vs. RHE) in an N_2-saturated 1 M KOH solution at a rotation rate of 1600 rpm. At the ring, a potential of 0.4 V vs. RHE was applied to investigate possible side reaction Scan rate of the disk electrode was set at 2 mV s^{-1}.

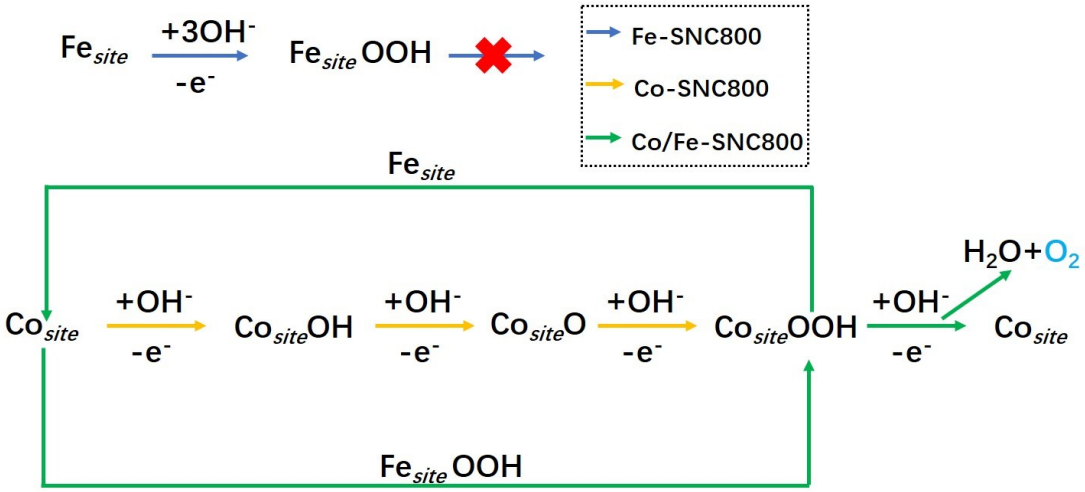

Figure 19. The scheme of the catalytic mechanism. The OER catalytic process occurs on Fe-SNC800, Co-SNC800, and Co/Fe-SNC800 via Equation S8, Equation S9-12, and Equation S8/S13/S14, respectively.

$$Fe_{site} + 3OH^- - 3e^- = Fe_{site}OOH + H_2O$$ (Equation S8)

$$Co_{site} + OH^- - e^- = Co_{site}OH$$ (Equation S9)

$$Co_{site}OH + OH^- - e^- = Co_{site}O + H_2O$$ (Equation S10)

$$Co_{site}O + OH^- - e^- = Co_{site}OOH$$ (Equation S11)

$$Co_{site}OOH + OH^- - e^- = Co_{site} + O_2 + H_2O$$ (Equation S12)

$$Fe_{site}OOH + Co_{site} = Co_{site}OOH + Fe_{site}$$ (Equation S13)

$$Co_{site}OOH + OH^- - e^- = Co_{site} + O_2 + H_2O$$ (Equation S14)

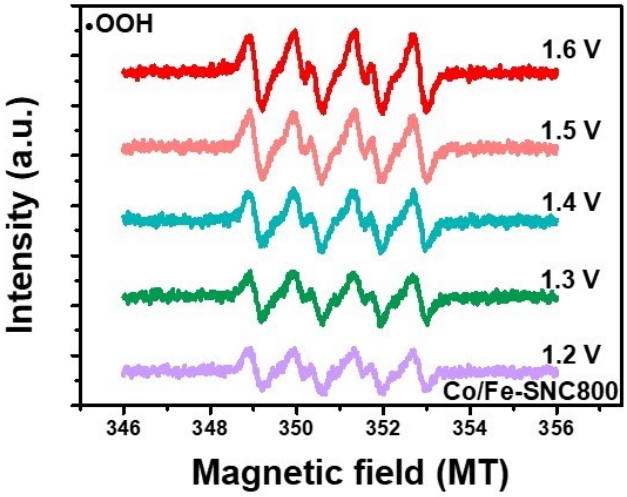

Figure S20. The EPR signals for *OOH with various applied potentials.

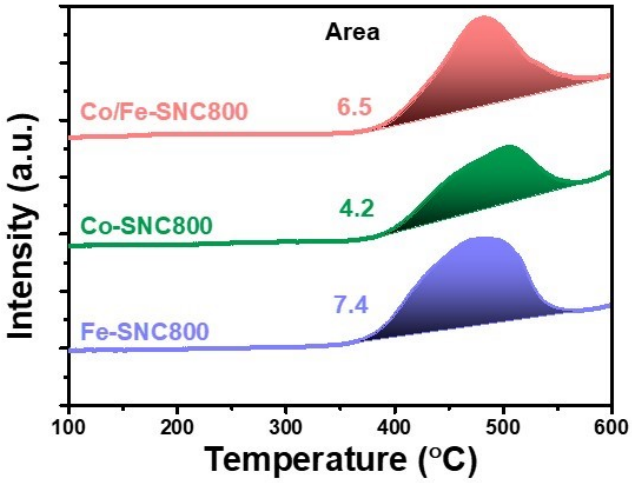

Figure S21. O_2-TPD of Fe-SNC800, Co-SNC800 and Co/Fe-SNC800, respectively.

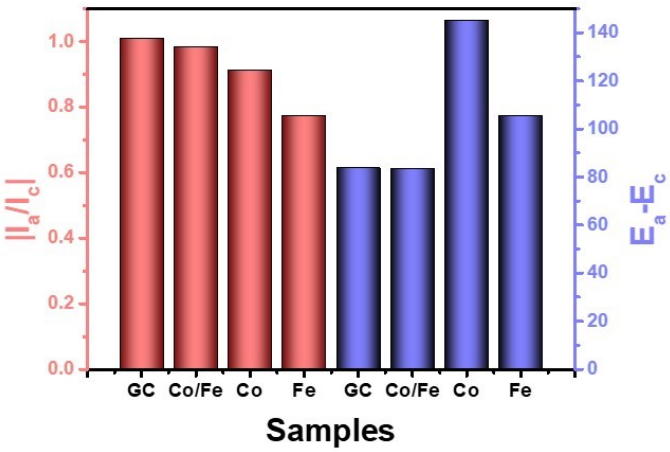

Figure S22. The I_a/I_c and E_a-E_c values of Fe-SNC800, Co-SNC800 and Co/Fe-SNC800, which are the oxidation/reduction current and oxidation/reduction potential of $K_3[Fe(CN)_6]/K_4[Fe(CN)_6]$ derived from the CV curves (Figure 4g). The I_a/I_c value of Co/Fe-SNC800 is similar to that of GC

(bare glass carbon) which is close to 1, indicating the fast electron transfer of the Co/Fe-SNC800. And the E_a-E_c value of Co/Fe-SNC800 also shows the favor electron transfer capacity.

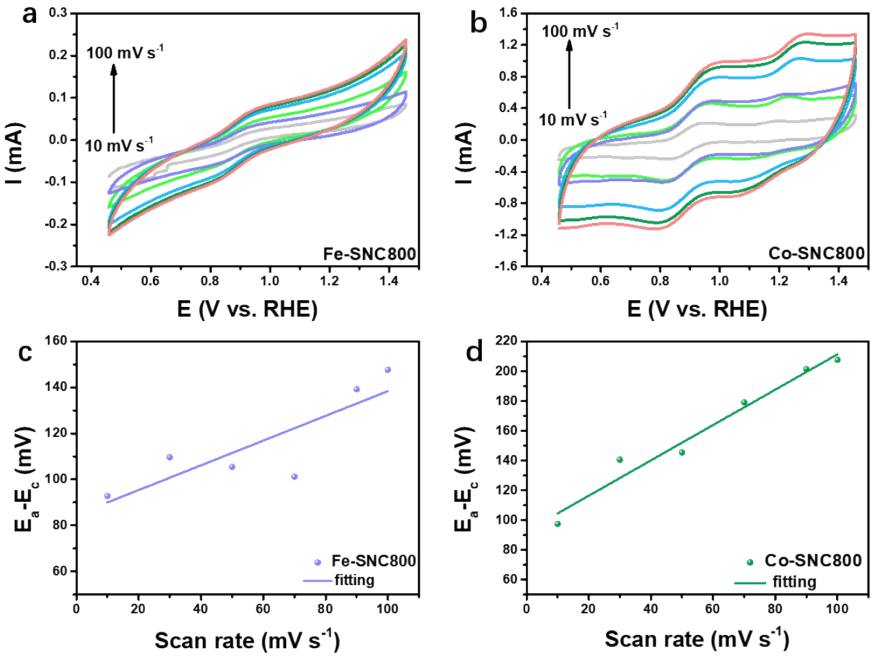

Figure S23. The CV curves of (a) Fe-SNC800 and (b) Co-SNC800 at the various scan rates of 10 mV s^{-1}, 30 mV s^{-1}, 50 mV s^{-1}, 70 mV s^{-1}, 90 mV s^{-1}, and 100 mV s^{-1} after conducting fifty cyclic voltammograms (CVs) at a scan rate of 200 mV s^{-1} in N_2-saturated 0.1 M KCl with 0.05 M $K_3[Fe(CN)_6]/K_4[Fe(CN)_6]$; (b) The plots of E_a-E_c value vs. scan rates for (c) Fe-SNC800 and (d) Co-SNC800. A new redox peak between 1.05 and 1.25 V of Co-SNC800 is attributed to the Co^{2+}/Co^{3+} redox pair. It is difficult to test for corresponding changes to the Fe redox pair since Fe does not exhibit clear reversible redox waves in the experimentally accessible electrochemical window.

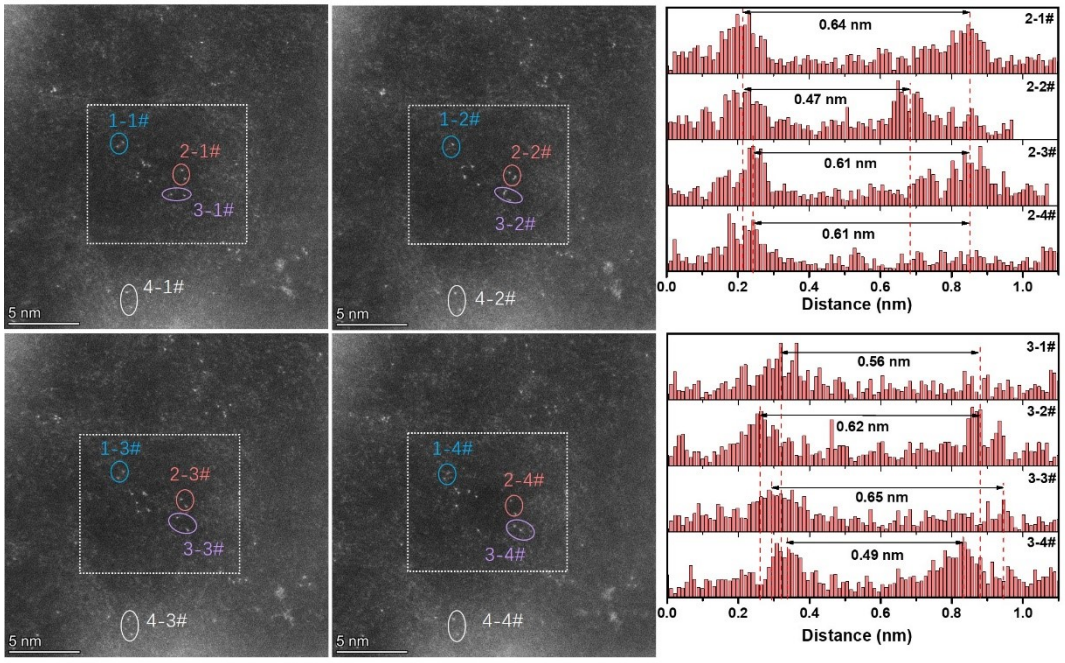

Figure S24. HAADF-STEM images of Co/Fe-SNC800 and corresponding intensity profiles along

the arrow in Region 2 and 3, respectively (the four pictures have been captured in less than 2 seconds).

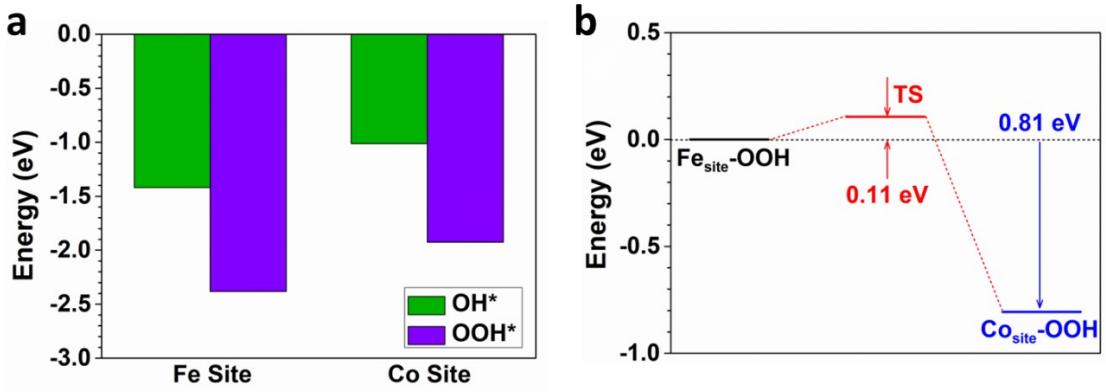

Figure S25. (a) Adsorption energy comparisons of OH* and O* on Fe and Co sites in Co/Fe-SNC. (b) The energy change for OOH* transfers from the Fe site to the Co site.

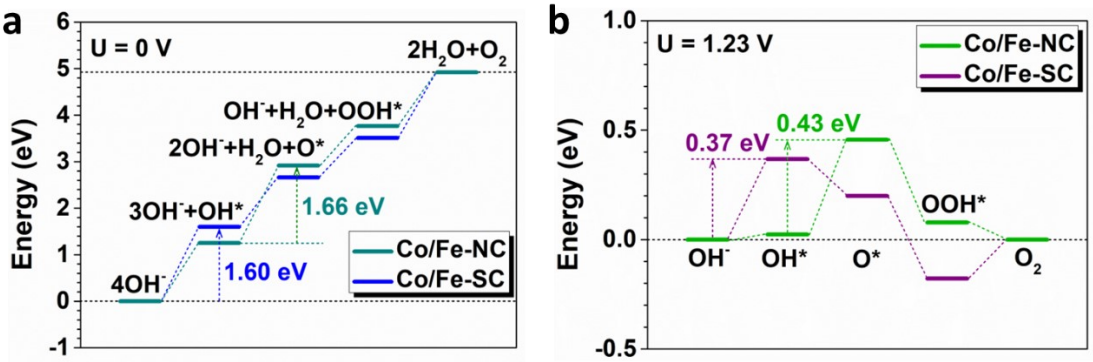

Figure S26. The reaction energy comparisons of OER for Co/Fe NC and Co/SC at (a) U= 0 V and (b) U = 1.23 V.

Table S1. The naming rules for the pre-catalysts.

Samples	Co/Fe precursor ratios	Pyrolysis temperature(°C)
Fe-SNC800	1:0	800
Co-SNC800	0:1	800
Co/Fe-SNC800(0.5:1)	0.5:1	800
Co/Fe-SNC800(0.6:1)	0.6:1	800
Co/Fe-SNC800(0.8:1)	0.8:1	800
Co/Fe-SNC800	**1:1**	800
Co/Fe-SNC800(1.2:1)	1.2:1	800
Co/Fe-SNC800(1.4:1)	1.4:1	800
Co/Fe-SNC800(1.6:1)	1.6:1	800
Co/Fe-SNC700	1:1	700
Co/Fe-SNC900	1:1	900

Table S2. Element composition measured by ICP-OES and element analysis of pre-catalysts.

Samples	Fe (wt%)	Co (wt%)	C (wt%)	N (wt%)	S (wt%)	O (wt%)
Fe-SNC800	1.09	-	53.61	16.74	5.45	10.20
Co-SNC800	-	1.24	57.56	16.79	1.83	12.66
Co/Fe-SNC800	1.18	1.66	59.86	10.57	4.21	14.37
Co/Fe-SNC800(0.5:1)	1.76	3.521	-	-	-	-
Co/Fe-SNC800(0.6:1)	1.63	3.05	-	-	-	-
Co/Fe-SNC800(0.8:1)	1.71	3.07	-	-	-	-
Co/Fe-SNC800(1.2:1)	1.78	1.83	-	-	-	-
Co/Fe-SNC800(1.4:1)	2.60	2.48	-	-	-	-
Co/Fe-SNC800(1.6:1)	4.21	2.66	-	-	-	-

Table S3. The reference OER catalytic activity of the reported single-atom catalysts or dual-atom

catalysts.

Catalysts	Overpotential @10 mA cm^{-2} (mV)	Tafel ($mV\ dec^{-1}$)	Ref.
Co/Fe-SNC800	240	47.92	This work
Co-Fe-N-C	320	34	[14]
CoFe-LDHs	310	59	[15]
Fe_2-GNCL	355	66	[16]
Fe_1/Co_1-GNCL	>480	129	[16]
Fe-Ni-N-C	395	100	[17]
Fe-Ni-N-P-C	335	76	[17]
NiFe@PCN	310	38	[18]
IrFe-N-C	350	43	[19]
CoNi-SAs/NC	340	58.7	[20]
Fe-NiNC-50	340	54	[21]
Ni SAs/Fe-NiOOH	269	33.4	[22]
CoSAs-NGST	560	-	[23]
Mo-CoOOH	249	60.5	[24]
W-CoOOH	330	91.1	[24]
Ni SAs@S/N-CMF	285	50.8	[25]

Table S4. The various parameters of Fe-SNC800, Co-SNC800, and Co/Fe-SNC800.

Samples	C_s ($mF\ mg_{cat}^{-1}\ cm^{-2}$)	C_{dl} ($mF\ cm^{-2}$)	ECSA (g_{cat}^{-1})	MASD (mol_{metal}^{-1})	Coefficient
Fe-SNC800	262.17	3.9	0.0149	4.05×10^{22}	7.4
Co-SNC800	351.00	18.0	0.0513	5.02×10^{22}	4.2
Co/Fe -SNC800	322.39	20.8	0.0645	1.15×10^{23}	6.5

6. References

1. M. F. Sanad, A. R. Puente Santiago, S. A. Tolba, M. A. Ahsan, O. Fernandez-Delgado, M. Shawky Adly, E. M. Hashem, M. Mahrous Abodouh, M. S. El-Shall, S. T. Sreenivasan, N. K. Allam and L. Echegoyen, *J. Am. Chem. Soc.*, 2021, **143**, 4046-4073.
2. M. L. Rigsby, D. J. Wasylenko, M. L. Pegis and J. M. Mayer, *J.Am.Chem.Soc.*, 2015, **137**, 4296-4299.
3. L. Yu, Y. Xiao, C. Luan, J. Yang, H. Qiao, Y. Wang, X. Zhang, X. Dai, Y. Yang and H. Zhao, *ACS Appl. Mater. Interfaces*, 2019, **11**, 6890-6899.
4. R. Zhou, Y. Zheng, M. Jaroniec and S.-Z. Qiao, *ACS Catal.*, 2016, **6**, 4720-4728.
5. T. Marshall-Roth, N. J. Libretto, A. T. Wrobel, K. J. Anderton, M. L. Pegis, N. D. Ricke, T. V. Voorhis, J. T. Miller and Y. Surendranath, *Nat. Commun.*, 2020, **11**, 5283.
6. E. Andriukonis, A. Ramanaviciene and A. Ramanavicius, *Polymers*, 2018, **10**, 749.
7. S. J. Clark, M. D. Segall, C. J. Pickard, P. J. Hasnip, M. J. Probert, K. Refson and M. C. Payne, *Z Kristallogr*, 2005, **220**, 567-570.
8. J. P. Perdew, K. Burke and M. Ernzerhof, *Phys. Rev. Lett.*, 1996, **77**, 3865-3868.
9. P. J. Hasnip and C. J. Pickard, *Comput. Phys. Commun.*, 2006, **174**, 24-29.
10. J. P. Perdew, J. A. Chevary, S. H. Vosko, K. A. Jackson, M. R. Pederson, D. J. Singh and C. Fiolhais, *Phys. Rev. B*, 1992, **46**, 6671-6687.
11. J. D. Head and M. C. Zerner, *Chem. Phys. Lett.*, 1985, **122**, 264-270.
12. Q. Wang, C. Q. Xu, W. Liu, S. F. Hung, H. Bin Yang, J. Gao, W. Cai, H. M. Chen, J. Li and B. Liu, *Nat. Commun.*, 2020, **11**, 4246.
13. W. Li, S. Watzele, H. A. El-Sayed, Y. Liang, G. Kieslich, A. S. Bandarenka, K. Rodewald, B.

Rieger and R. A. Fischer, *J. Am. Chem. Soc.*, 2019, **141**, 5926-5933.

14. L. Bai, C. S. Hsu, D. T. L. Alexander, H. M. Chen and X. Hu, *J. Am. Chem. Soc.*, 2019, **141**, 14190-14199.
15. P. Li, M. Wang, X. Duan, L. Zheng, X. Cheng, Y. Zhang, Y. Kuang, Y. Li, Q. Ma, Z. Feng, W. Liu and X. Sun, *Nat. Commun.*, 2019, **10**, 1711.
16. Y. S. Wei, L. Sun, M. Wang, J. Hong, L. Zou, H. Liu, Y. Wang, M. Zhang, Z. Liu, Y. Li, S. Horike, K. Suenaga and Q. Xu, *Angew. Chem. Int. Ed. Engl.*, 2020, **59**, 16013-16022.
17. F. Pan, T. Jin, W. Yang, H. Li, Y. Cao, J. Hu, X. Zhou, H. Liu and X. Duan, *Chem Catalysis*, 2021, **1**, 734-745.
18. C. Wu, X. Zhang, Z. Xia, M. Shu, H. Li, X. Xu, R. Si, A. I. Rykov, J. Wang, S. Yu, S. Wang and G. Sun, *J. Mater. Chem. A*, 2019, **7**, 14001-14010.
19. Z. Yu, C. Si, A. P. LaGrow, Z. Tai, W. A. Caliebe, A. Tayal, M. J. Sampaio, J. P. S. Sousa, I. Amorim, A. Araujo, L. Meng, J. L. Faria, J. Xu, B. Li and L. Liu, *ACS Catal.*, 2022, **12**, 9397-9409.
20. X. Han, X. Ling, D. Yu, D. Xie, L. Li, S. Peng, C. Zhong, N. Zhao, Y. Deng and W. Hu, *Adv. Mater.*, 2019, **31**, e1905622.
21. X. Zhu, D. Zhang, C.-J. Chen, Q. Zhang, R.-S. Liu, Z. Xia, L. Dai, R. Amal and X. Lu, *Nano Energy*, 2020, **71**, 104597.
22. H. Liu, X. Xu, H. Xu, S. Wang, Z. Niu, Q. Jia, L. Yang, R. Cao, L. Zheng and D. Cao, *Applied Catalysis B: Environmental*, 2021, **297**, 120451.
23. J. J. Ban, X. H. Wen, H. J. Xu, Z. Wang, X. H. Liu, G. Q. Cao, G. S. Shao and J. H. Hu, *Adv. Funct. Mater.*, 2021, **31**, 2010472.
24. L. Tang, L. Yu, C. Ma, Y. Song, Y. Tu, Y. Zhang, X. Bo and D. Deng, *J. Mater. Chem. A*, 2022, **10**, 6242-6250.
25. Y. Zhao, Y. Guo, X. F. Lu, D. Luan, X. Gu and X. W. D. Lou, *Adv. Mater.*, 2022, **34**, e2203442.